ACS APPLIED MATERIALS & INTERFACES

Research Article

Cite This: ACS Appl. Mater. Interfaces 2018, 10, 10211−10219

www.acsami.org

Manipulating the Structural and Electronic Properties of Epitaxial $SrCoO_{2.5}$ Thin Films by Tuning the Epitaxial Strain

Jiali Zhao,[†,‡,⊥] Haizhong Guo,[*,†,§] Xu He,[†] Qinghua Zhang,[†,⊥] Lin Gu,[†,⊥] Xiaolong Li,[∥] Kui-juan Jin,[*,†,⊥] Tieying Yang,[∥] Chen Ge,[†] Yi Luo,[§] Meng He,[†] Youwen Long,[†,⊥] Jia-ou Wang,[‡] Haijie Qian,[‡] Can Wang,[†] Huibin Lu,[†] Guozhen Yang,[†,⊥] and Kurash Ibrahim[*,‡]

[†]Institute of Physics, Chinese Academy of Sciences, Beijing 100190, China

[‡]Beijing Synchrotron Radiation Facility Institute of High Energy Physics, Chinese Academy of Sciences, Beijing 100049, China

[§]School of Physical Engineering, Zhengzhou University, Zhengzhou, Henan 450001, China

[∥]Shanghai Synchrotron Radiation Facility (SSRF), Shanghai Institute of Applied Physics, Chinese Academy of Sciences, Shanghai 201204, China

[⊥]University of Chinese Academy of Sciences, Beijing 100049, China

Supporting Information

ABSTRACT: Structure determines material's functionality, and strain tunes the structure. Tuning the coherent epitaxial strain by varying the thickness of the films is a precise route to manipulate the functional properties in the low-dimensional oxide materials. Here, to explore the effects of the coherent epitaxial strain on the properties of $SrCoO_{2.5}$ thin films, thickness-dependent evolutions of the structural properties and electronic structures were investigated by X-ray diffraction, Raman spectra, optical absorption spectra, scanning transmission electron microscopy (STEM), and first-principles calculations. By increasing the thickness of the $SrCoO_{2.5}$ films, the *c*-axis lattice constant decreases, indicating the relaxation of the coherent epitaxial strain. The energy band gap increases and the Raman spectra undergo a substantial softening with the relaxation of the coherent epitaxial strain. From the STEM results, it can be concluded that the strain causes the variation of the oxygen content in the BM-SCO2.5 films, which results in the variation of band gaps with varying the strain. First-principles calculations show that strain-induced changes in bond lengths and angles of the octahedral CoO_6 and tetrahedral CoO_4 cannot explain the variation band gap. Our findings offer an alternative strategy to manipulate structural and electronic properties by tuning the coherent epitaxial strain in transition-metal oxide thin films.

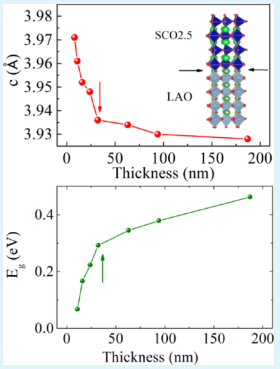

KEYWORDS: *$SrCoO_{2.5}$ thin films, epitaxial strain, electronic structure, Raman scattering, first-principle calculations*

1. INTRODUCTION

Strongly correlated transition-metal oxides (TMOs) have attracted enormous attention owing to their peculiar properties, such as superconductivity in the cuprates, colossal magnetoresistance in the manganites, ferroelectricity in the titanates, and so on.[1] All these unique properties are attributed to coupling of charge, spin, lattice, and orbital degrees of freedom. Dynamically tuning oxygen vacancies and strain can influence the coupling of charge, spin, lattice, and orbital degrees of freedom, thus providing routes to create new functionalities.[2−7] On the other hand, the lack of fossil fuels and the environmental problems promote the development of environmentally friendly and renewable energy applications. TMOs with mixed valence states can be applied in these fields, such as catalysts, oxygen separation membranes, hydrogen generation from water splitting, cathodes in rechargeable batteries, solid oxide fuel cells, and so on.[8−20] Co-based oxides are the most promising candidates for solar thermochemical energy storage application.[21−25] With the variation of the oxygen stoichiometry, ferromagnetic metal perovskite $SrCoO_3$ and antiferromagnetic insulator brownmillerite $SrCoO_{2.5}$(BM-SCO2.5) can be transferred from one crystalline phase to the other one fast at low temperatures because of the small Gibbs free-energy difference between the two topotatic phases.[7,26−32] Recently, Yu et al. have performed an electric field to drive reversible tristate phase transformations among three different material phases: $SrCoO_3$, $SrCoO_{2.5}$, and new-explored weakly ferromagnetic insulating phase $HSrCoO_{2.5}$ by controlling the insertion and extraction of oxygen and hydrogen ions independent of each other.[33] The migration of oxygen vacancy by electrical induction and the reconstructive structural transformation in $SrCoO_{2.5-\delta}$ were observed by the scanning transmission electron microscopy (STEM) technique.[34] Among a variety of phases with rich functionality of Co-based oxides, BM-SCO2.5 due to its exotic structure and properties attracts more and more attention and research. BM-SCO2.5 shows

Received: January 17, 2018
Accepted: March 7, 2018
Published: March 7, 2018

DOI: 10.1021/acsami.8b00791
ACS Appl. Mater. Interfaces 2018, 10, 10211−10219

alternating octahedral CoO_6 and tetrahedral CoO_4 layers, which has well-ordered one-dimensional oxygen vacancies within the tetrahedral layer that are absent within its perovskite counterpart. The well-ordered oxygen vacancies in BM-SCO2.5 are beneficial for the oxygen diffusion and anisotropic ionic conduction, which is useful for the enhancement of the efficacy of electrocatalysts and the development of solid oxide fuel cells.[8,35−37] Mefford et al. have explored the water electrolysis on $La_{1-x}Sr_xCoO_{3-\delta}$ perovskite electrocatalysts and demonstrated that through the modulation of the Fermi energy through transition-metal 3d and oxygen 2p partial density of states by the oxygen vacancies, the electrocatalysis of oxygen on metal oxide surfaces can be improved.[38] Jeen et al. have reported that the topotatic SCO2.5 film which has the oxygen vacancy channels terminated at the surface can enhance the catalytic reaction dramatically.[8]

Moreover, epitaxial strain due to the lattice mismatch is an essential route to tune the properties of thin films.[39,40] Oxygen content of $SrCoO_x$ can be manipulated by the strain through epitaxially grown on different lattice-mismatched substrates.[41,42] Bulk $LaCoO_3$ is nonmagnetic, whereas thin film shows a long-range ferromagnetic ordering below 80 K.[43] Meyer et al. have reported the interfacial and bulk structure of BM-SCO2.5 thin films grown on the $SrTiO_3$ (STO) substrates.[44] From first-principles calculation, the strain including tensile and compressive can drive perovskite $SrCoO_3$ bulk from the ferromagnetic-metal phase to the antiferromagnetic-insulator-ferroelectric phase.[45] Despite theoretical and experimental efforts to investigate the effects of the strain on the properties of perovskite $SrCoO_x$ and $LaCoO_3$, there are no literature studies that have reported the influence of the coherent strain on the properties of the BM-SCO2.5 thin films.

In this work, a series of the BM-SCO2.5 thin films with different thicknesses to vary the epitaxial strain were grown by pulsed laser deposition (PLD). The evolutions of the structural and electronic properties were investigated by X-ray diffraction, optical absorption spectra, Raman scattering, STEM, electric transport measurement, and magnetic measurement. With the increase of film thicknesses, the coherent epitaxial strain from the substrate relaxes, and the energy band gap of BM-SCO2.5 thin film increases, the Raman spectra undergo a substantial softening. The experimental results can be well-understood by the theoretic calculation.

2. EXPERIMENTAL SECTION

2.1. Fabrication of SCO2.5 Films. Epitaxial SCO2.5 thin films with various thicknesses of 8, 11, 16, 24, 32, 63, 94, and 187 nm were deposited on (001)-oriented $LaAlO_3$ (LAO) by PLD. The films were deposited at 700 °C using an excimer XeCl laser (1.5 J/cm^2, 308 nm, 2 Hz) at an oxygen pressure of 10 Pa. After deposition, the films were in situ annealed for 30 min and then cooled down slowly to room temperature; the whole process was carried out at the oxygen pressure of 10 Pa.

2.2. X-ray Diffractometry (XRD), Raman, and Optical Absorption Spectral Measurements. The structural phases and out-of-plane lattice constant of the SCO2.5 thin films were identified by XRD. XRD data were collected with a Rigaku SmartLab (9 kW) high-resolution (Ge 220 × 2) X-ray diffractometer with 1.54 Å X-rays. The temperature-dependent measurement of the lattice constants of the SCO2.5 thin film were performed by high-resolution synchrotron XRD at the BL14B1 beam line of Shanghai Synchrotron Radiation Facility (SSRF) using a 1.24 Å X-rays with a Huber 5021 six-axis diffractometer. Raman spectroscopy was conducted on a Horiba Jobin Yvon Lab RAM HR-800 Raman microscope under ambient conditions at room temperature. The excitation light is a 532 nm laser, with a laser power of 1 mW and an estimated beam spot size of 1 μm^2. Optical absorption of thin films was measured in the wavelength range of 400−3100 nm using a UV−vis−NIR spectrophotometer (Varian Cary 5000).

2.3. STEM Measurements. The atomic structure of two different thickness SCO2.5 thin films was characterized using an ARM-200CF (JEOL, Tokyo, Japan) transmission electron microscope operated and equipped with double spherical aberration (Cs) correctors.

2.4. First-Principles Calculations. The density functional theory (DFT) calculations based on planewave basis set, projected augmented wave potentials, and PBEsol exchange correlation functional were carried out with the VASP package. A DFT + U (U(Co) = 3.5 eV) correction is used to better describe the on-site electron−electron interaction in transitional-metal atoms. A 4 × 4 × 3 γ-centered K-mesh grid was used. The strain effect is simulated by fixing the ab lattice constants with c relaxed.

3. RESULTS AND DISCUSSION

3.1. Structural Evolutions Investigated by XRD. Epitaxial SCO2.5 thin films with various thicknesses were deposited on the LAO single crystals by PLD. Details on film growth are given in the Experimental Section. The temperature dependent results of magnetization and electronic transport properties (Figures S1 and S2) indicate that the 187 nm-thick SCO2.5 thin film is an antiferromagnetic insulator, which are consistent with the previous reports.[7,29]

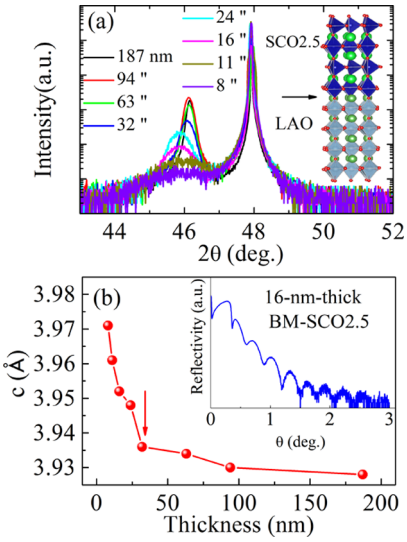

Figure 1. (a) XRD θ−2θ patterns of c-axis-oriented BM-SCO2.5 films with the different thicknesses of 8, 11, 16, 24, 32, 63, 94, and 187 nm, respectively. (b) Variation of the lattice constant c with the film thicknesses; the inset showing the X-ray reflectivity profile of the 16 nm-thick BM-SCO2.5 thin film.

To characterize the quality of films, XRD data of the BM-SCO2.5 thin films were measured. The XRD results confirmed that SCO films are c-axis-oriented and at single phase, and the XRD confirms the coherent growth on the LAO substrate (see Figure S3). Figure S4 exhibits the XRD θ−2θ patterns of the BM-SCO2.5 films on (001) LAO substrates with different thicknesses of 8, 11, 16, 24, 32, 63, 94, and 187 nm, respectively. Figure 1a shows the enlarged part of Figure S4. It can be seen from Figure 1a that all the films with the thicknesses from 8 to 187 nm are at single-phase and the (008) peak shifts toward high 2θ angle with the increase of the film thickness. The inset of Figure 1b shows the X-ray reflectivity profile of 16 nm-thick BM-SCO thin films. The thickness of the

DOI: 10.1021/acsami.8b00791
ACS Appl. Mater. Interfaces 2018, 10, 10211−10219

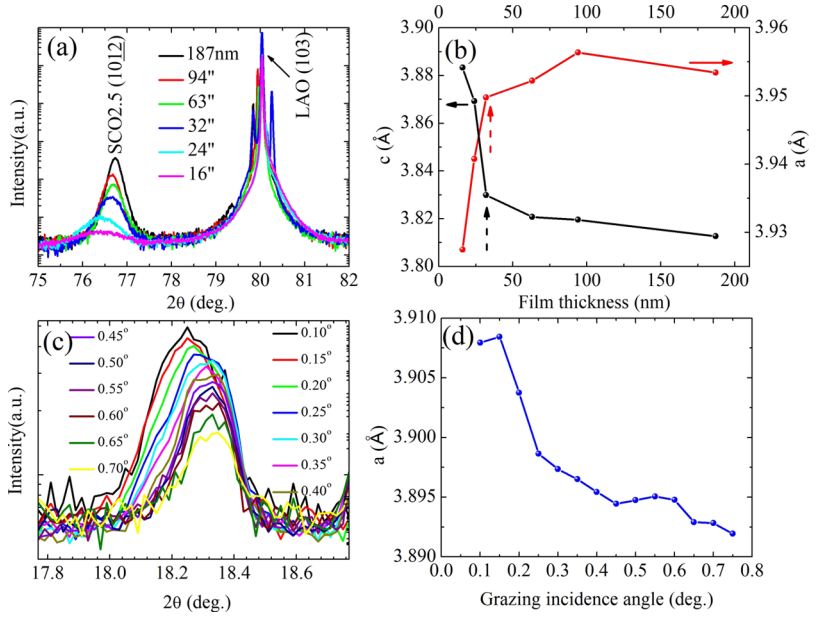

Figure 2. (a) XRD θ–2θ scan of BM-SCO2.5 films with different thicknesses around the (103) LAO substrate. (b) Variation of the lattice constant c and a with the film thicknesses. (c) Grazing incidence XRD of 187 nm BM-SCO2.5 with different grazing incidence angles. (d) Variation of lattice constant a of 187 nm BM-SCO2.5 with different grazing incidence angles.

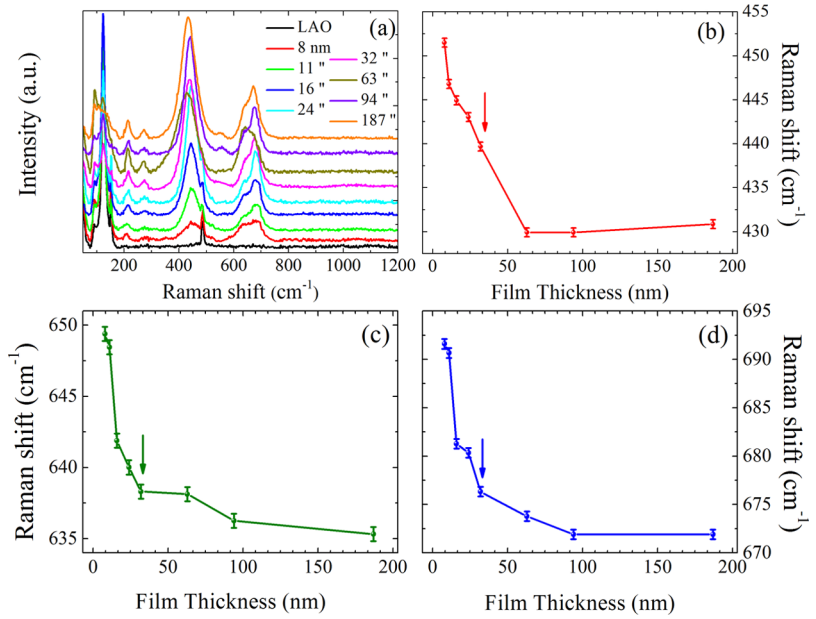

Figure 3. (a) Raman spectra of the different thicknesses of the SrCoO2.5 thin film and the LAO substrate. (b–d) Relations of the film thicknesses and the peak positions of 450, 650, and 690 cm^{-1} modes, respectively.

SCO thin film was obtained from the periodicity of the interference fringes. The c-axis lattice constant of the BM-SCO2.5 thin films with the different thicknesses can be calculated from the θ–2θ scans (Figure 1a). The variation of c-axis lattice constant c as a function of the film thickness is shown in Figure 1b. It can be seen from Figure 1b that with the increase of the film thickness from 8 nm, the lattice constant c decreases quickly and then decreases smoothly when the BM-SCO thickness is larger than 40 nm, indicating that the thickness of 40 nm is a critical point (black dash arrow). However, the lattice constant a, in contrary, increases quickly and then smoothly with the increase of the BM-SCO thickness, and the thickness of 40 nm is also the critical point (red dash arrow). LAO is a cubic cell with the lattice constant ~3.792 Å. BM-SCO2.5 is orthorhombic unit cell with a = 5.574 Å, b = 5.470 Å, c = 15.745 Å, which can be seen as a pseudotetragonal structure with lattice constants a = 3.905 Å, c = 3.936 Å. Because of the lattice mismatch (+2.980%) between the BM-SCO thin film and the LAO substrate, in-plane epitaxial compressive strain and out-of-plane tensile strain were generated in the BM-SCO films from the interface when the BM-SCO films were grown on the LAO substrates, and the BM-SCO lattice is compressed in the in-plane direction and elongated in the out-of-plane direction. As the film thickness increases from a few nm, the strain will be released quickly, which results in the quick decrease of the lattice constant c.

DOI: 10.1021/acsami.8b00791
ACS Appl. Mater. Interfaces 2018, 10, 10211–10219

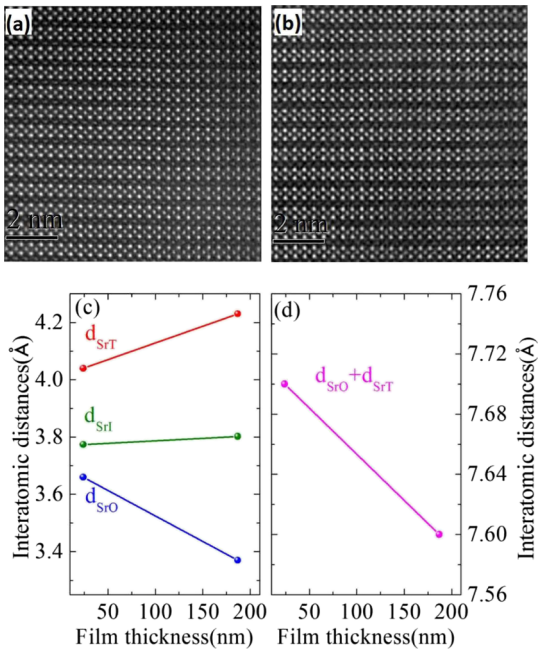

Figure 4. HAADF measurements for two different thicknesses of BM-SCO: (a) 24 nm and (b) 187 nm and (c,d) Sr−Sr distances. In-plane Sr−Sr distance d_{SrI} (green) and two types of out-of-plane Sr−Sr: d_{SrT} (red) and d_{SrO} (blue).

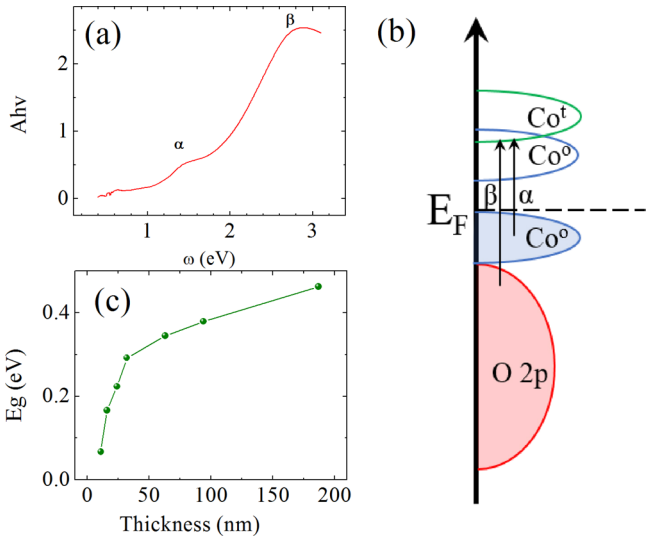

Figure 5. (a) Optical absorption spectrum obtained from transmittance measurements of the SrCoO2.5 thin films. (b) Schematic band diagrams of BM-SCO2.5. (c) Energy band gap of the SrCoO2.5 thin films with different thicknesses obtained from optical absorption spectra.

When the film thickness reaches the critical point, ~40 nm, the strain almost completely releases, and *c* decreases slowly with further increasing thickness.

We also measured the XRD patterns of the BM-SCO films with different thicknesses around the (103) LAO substrate, as shown in Figure 2a. The *a*-axis lattice constant of the BM-SCO2.5 thin films with the different thicknesses can be calculated from Figures 1a and 2a. Figure 2b shows the variation of lattice constants *c* and *a* with the film thickness. The grazing incidence XRD of the 187 nm-thick BM-SCO2.5 film with different grazing incidence angles is shown in Figure 2c. It can be seen from Figure 2d that with the increase of the incidence angle, the lattice constant *a* decreases, which indicates that with increasing thickness, the strain releases. The full width at half-maximum (fwhm) of (008) peak decreases with the increase of the film thickness also indicates the existence of strain (see Figure S5). In this work, the coherent epitaxial strain makes a big difference to the structure of BM-SCO2.5, which we will discuss in detail.

3.2. Phonon Evolution with the Thicknesses Investigated by Raman Scattering. Raman spectrum is an effective tool to observe vibration and rotation of molecules or atoms in a system.[46] The Raman shift gives information about the vibrational modes in the system. To get information about the effects of the strain on the structural properties in the BM-SCO thin films, Raman spectra of the BM-SCO2.5 thin films with the different thicknesses were performed, as shown in Figure 3a. For the crystal structure symmetry of the BM-SCO2.5 bulk, there are three space groups including *Imma*, *Ima*2, and *Pnma* that have been proposed and discussed.[47,48] Glamazda et al. have confirmed that only *Imma* reproduces the observed Raman-active phonons of the BM-SCO2.5 thin films on the $(LaAlO_3)_{0.3}-(SrAlTaO_3)_{0.7}$ (LSAT) substrates after detailed analysis of the phonon modes by the Raman scattering experiments and lattice dynamic calculations.[49] It can be seen from Figure 3a that except the Raman mode ~120 cm^{-1} coming from the LAO substrates, there are two small modes located at 218 and 273 cm^{-1} and two broad modes located at 400−500 and 600−700 cm^{-1}. Two small modes can be assigned to P5(1)/P5(2) mode and P6(1)/P6(2) mode, respectively, according to the results of the Raman scattering experiments and lattice calculations.[49] The broad mode ~400−500 cm^{-1} is assigned to P7(1)/P7(2)/P7(3)/P7(4) mode. The broad mode of 600−700 cm^{-1} can be ascribed to two-phonon scattering, P10 and P11 modes, which are overtones and combinations.[49,50] From detailed lattice dynamic calculations in the literature,[49] the P7 mode (450 cm^{-1}) can be attributed to the mixed bending vibrations of the CoO_6 and CoO_4 tetrahedron, the P10 mode (650 cm^{-1}) involves out-of-phase stretching vibrations of apical O(2) in the *yz*-plane and out-of-phase motion of the Co(1) and Co(2) along the *z*-axis, and the P11 mode (690 cm^{-1}) is attributed to CoO_6 breathing and apical O(2) out-of-phase stretching in the *yz*-plane and Co(1) and Co(2) out-of-phase vibrations along the *y*-axis. Comparing our Raman scattering results and the results of Glamazda's work, it can be concluded that the space group of our BM-SCO2.5 films is *Imma*, which can be understood because the almost same lattice constants of the LAO substrate (3.792 Å) and the LSAT (3.868 Å) substrate and almost the same lattice mismatch between the films and substrates. All Raman modes exhibit a softening trend with increasing film thickness. To quantify the evolution of the Raman modes as a function of the film thickness, we fit the Raman spectra to a sum of the Lorentzian profiles, and the fitting results are shown in Figure 3b−d. It can be seen from Figure 3b−d, with the increase of the film thickness from 8 nm, the peak positions of the modes of 450 (P7), 650 (P10), and 690 (P11) cm^{-1} all shift toward low frequency quickly and then smoothly when the thickness of the BM-SCO2.5 film is larger than 40 nm, as same as the critical point of the complete release of the strain from the XRD results. This indicates that the thickness of 40 nm is a critical point for softening (arrows shown in Figure 3). The softening is about 20 cm^{-1}. The substantial softening of the Raman modes with the thickness indicates the strain release. The trend

DOI: 10.1021/acsami.8b00791
ACS Appl. Mater. Interfaces 2018, 10, 10211−10219

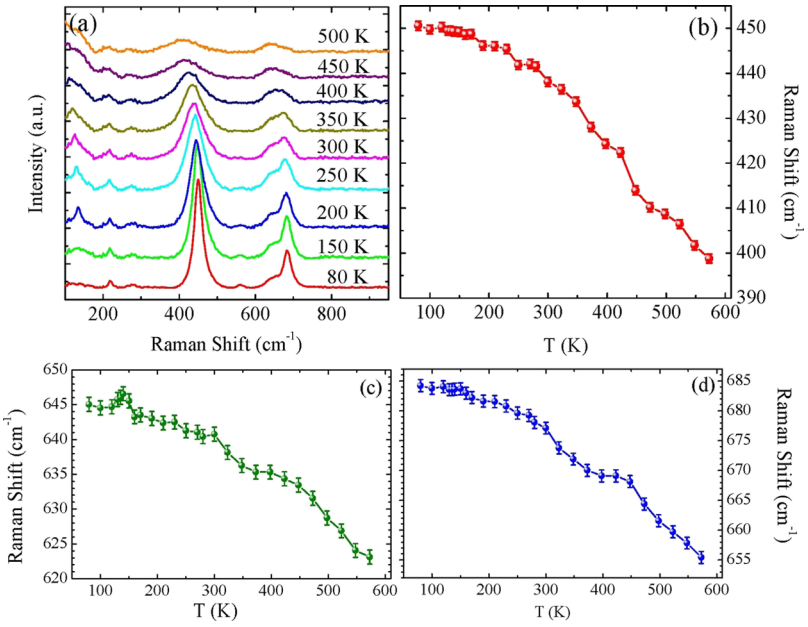

Figure 6. (a) Raman spectra of the 94 nm-thick SCO2.5 thin film measured at different temperatures from 80 to 500 K. (b–d) Temperature-dependent Raman peak positions of 450, 650, and 690 cm^{-1} modes, respectively.

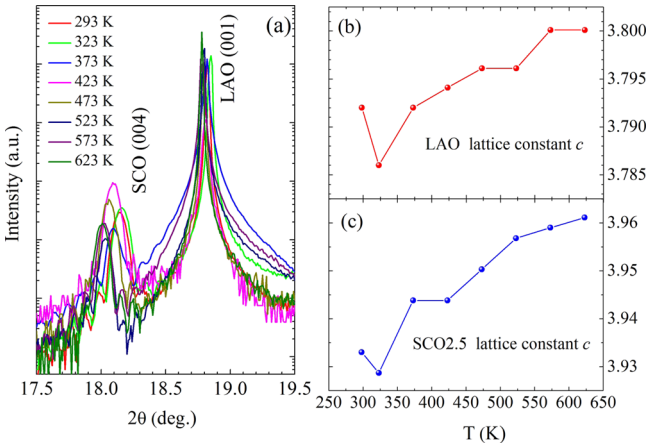

Figure 7. (a) XRD results of the 94 nm-thick SCO2.5 thin film measured at different temperatures from 293 to 623 K. (b,c) Temperature-dependent lattice constants c of the LAO substrate and the SCO2.5 film, respectively.

of the softening of the Raman mode with the film thickness is consistent with the XRD results, further confirming that the strain plays a key role on the structural properties of the BM-SCO thin films. The strain directly affects the bond lengths and angles of the octahedral CoO_6 and tetrahedral CoO_4 and then the vibrations and rotation of the Raman modes.

3.3. Local Structure Variation Investigated by STEM. Strain can directly affect the internal bond length and functionality, but also can create oxygen vacancies. To investigate whether the change of oxygen content or not, we performed the high-angle annular dark field (HAADF) STEM measurements of BM-SCO2.5 films with the thickness of 24 and 187 nm, as shown in Figure 4a,b, respectively. From Figure 4a,b, we can obtain the Sr–Sr distance including in-plane d_{SrI} and out-of-plane, as shown in Figure 4c,d. The out-of-plane consists of two types, d_{SrO} and d_{SrT}, which correspond to octahedral and tetrahedral layers, respectively. From Figure 4c, we can see that the d_{SrI} of 187 nm-thick BM-SCO2.5 film is bigger than that of the 24 nm-thick BM-SCO2.5 film, and the d_{SrO} and the $d_{SrO} + d_{SrT}$ of the 187 nm-thick BM-SCO2.5 film are smaller than that of the 24 nm-thick BM-SCO2.5 film, which indicates that with the increase of the film thickness, the strain releases. However, the d_{SrT} becomes bigger with the increase of the film thickness. In the $ACoO_{3-x}$ (A is alkaline earth of rare earth elements) system, oxygen vacancy would expand the lattice and a nearly linear relationship has been verified between the A–A cationic distance and the oxygen vacancy.[34] The d_{SrT} of the 187 nm-thick BM-SCO2.5 film is 4.23 Å, which is closer to $SrCoO_{2.5}$,[34] and therefore the 187 nm-thick BM-SCO2.5 is $SrCoO_{2.5}$, and the 24 nm-thick BM-SCO2.5 film is $SrCoO_{2.5+\delta}$.For different thickness films, strain not only tunes the structure but also changes the chemical stoichiometry.

3.4. Energy Band Gap Investigated by Optical Absorption. In materials, the structure determines functionality, and strain will tune the structure by directly affecting the internal bond length and angles and indirectly the variation of chemical stoichiometry. The variation of the lattice structure should make a big influence on the electronic structure and then the properties of the BM-SCO thin films. To shed more light on the influence of the strain on the electronic structure of the BM-SCO, the optical absorption spectra of the BM-SCO thin films were measured to investigate the change of energy band gap with the strain.

Figure 5a shows the optical absorption spectra obtained from transmittance measurements of the 187 nm-thick BM-SCO thin film at room temperature. It can be seen from Figure 5a that there are two characteristic peaks α and β, which represent a d–d transition between octahedral Co t_{2g} states and a transition between O 2p and mostly octahedral Co t_{2g} and e_g states, respectively.[32] Figure 5b shows the schematic band diagram of the BM-SCO2.5 thin film. Energy band gap can be obtained from optical absorption spectra. By plotting $(Ah\nu)^{1/2}$ and doing the tangent line near peak α, the intersection point of $y = 0$ and the tangent line is the energy band gap of the BM-SCO2.5 thin film. The optical absorption spectra of the BM-

DOI: 10.1021/acsami.8b00791
ACS Appl. Mater. Interfaces 2018, 10, 10211–10219

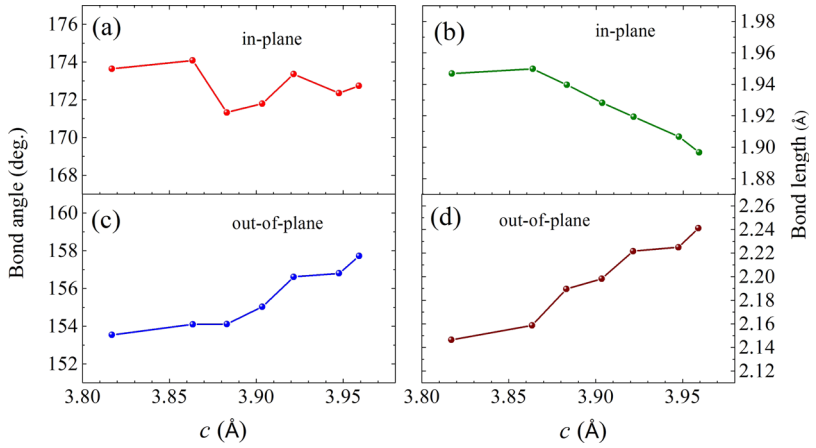

Figure 8. Calculation results of the variation of (a) Co−O bond angles and (b) lengths in octahedron in-plane with lattice constant *c*. Calculation results of the variation of (c) Co−O bond angles and (d) lengths in octahedron out-of-plane with lattice constant *c*.

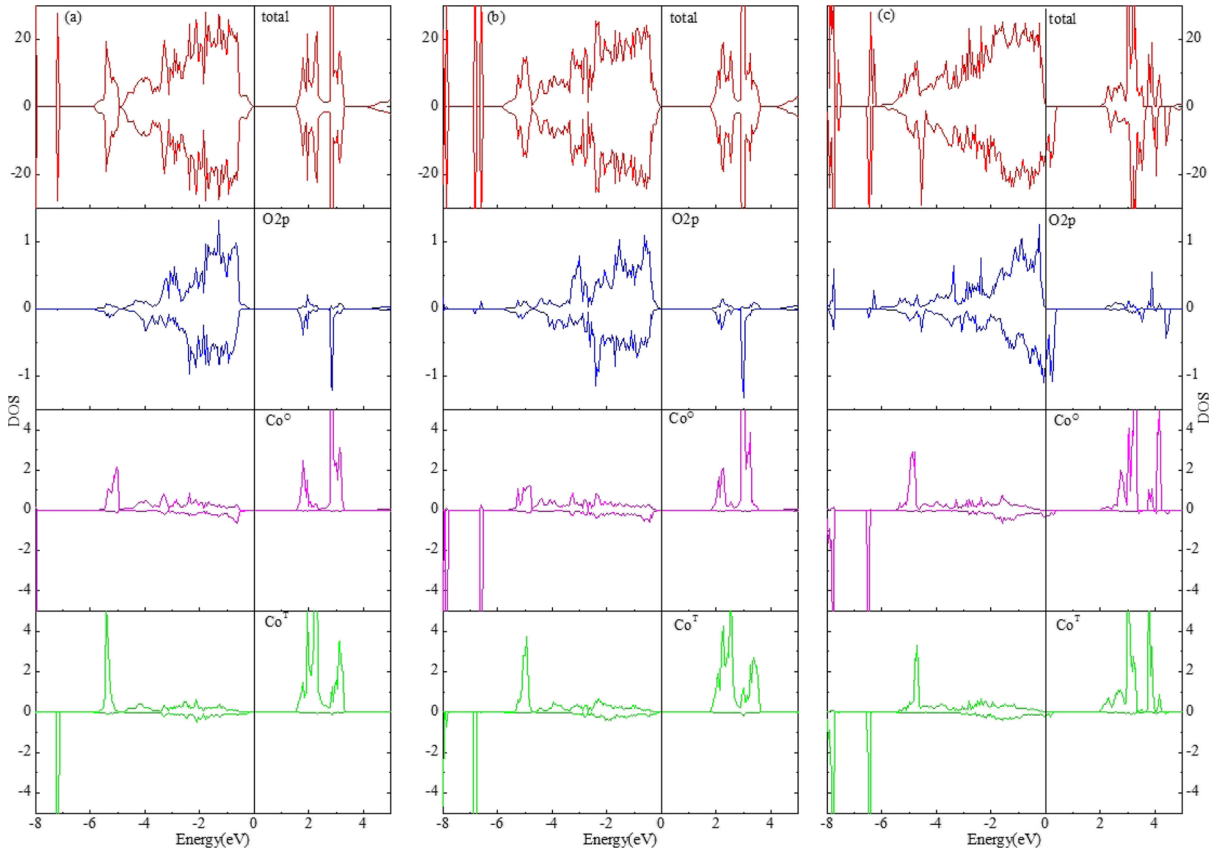

Figure 9. Total and projected DOS onto O 2p, Co-tetrahedral 3d and Co-octahedral 3d for the BM-SCO2.5 thin film with different lattice constants of (a) a = 3.810 Å, c = 3.947 Å, (b) a = 3.850 Å, c = 3.902 Å and (c) SrCoO2.75.

SCO2.5 thin films with the different thicknesses are shown in Figure S7, and the variation of obtained energy band gap with the thicknesses of the BM-SCO thin films is shown in Figure 5c. By increasing the film thickness from 11 nm, the energy band gap increase at first quickly and then smoothly after the thickness is larger than 40 nm. This trend is also consistent with the results of XRD and Raman scattering. This phenomenon should be related to the evolution of the lattice structure due to the strain.

3.5. Temperature-Dependent Raman Spectra and XRD. To investigate the temperature-dependent structures and strain, Raman spectra and XRD under different temperatures were performed. Figure 6a exhibits the temperature dependence of the Raman spectra for the 94 nm-thick SCO2.5 thin film. All Raman modes exhibit strong temperature dependences: the peaks become broad and weak, and the peak positions shift toward low wavenumber direction with increasing temperature. To investigate quantitatively the evolution of the peak frequencies, the spectra were fitted to the Lorentzian functions, and the fitting results for three different modes display in Figure 6b−d, respectively. It can be seen from Figure 6b−d that the softening of the Raman modes with increasing temperature is close to linear and the softening maybe come from the lattice expansion with temperature. The

DOI: 10.1021/acsami.8b00791
ACS Appl. Mater. Interfaces 2018, 10, 10211−10219

temperature-dependent Raman modes of the 32 nm-thick SCO2.5 thin film also exhibit similar behaviors, as seen in Figure S7. The temperature-dependent XRD measurement was performed, as shown in Figure 7a. Figure 7b,c shows the calculated lattice constant c of the LAO substrate and the SCO2.5 film from the XRD results, respectively. The relations of the temperature and the lattice constant c of the LAO substrate and the SCO2.5 film are both almost linear, shown in Figure 7b,c. It should be also noted from Figure 7b,c that the expansion of the lattice constant c of the SCO2.5 film is a little larger than that of the LAO substrate, indicating that the strain in the SCO2.5 film is more easily relaxed at high temperatures. Thermal expansion coefficient along the out-of-plane direction for SCO2.5 is experimentally determined to be 1.96×10^{-5} K^{-1}. However, the thermal expansion coefficient of LAO is 9.2×10^{-6} K^{-1}, a little smaller than that of SCO2.5, and therefore the SCO2.5 films increase faster than LAO with increasing temperature. Because of the similar temperature dependences of the Raman spectra and the lattice constants, the softening of the Raman modes may result from the lattice expansion with increasing temperature. This softening can be described approximately by the Grüneisen law $\Delta\nu/\nu = -\gamma\Delta V/V$ and by the usual phonon effects because of an anharmonicity of the lattice potential.[51]

3.6. Theoretical Calculation of the Evolution of the Electronic Structure with Strain. To unambiguously describe the relationship between the strain and the electron structures of the BM-SCO2.5 thin films, we calculated the relations of the Co−O bond angle and the lengths in octahedron in-plane and out-of-plane with the lattice constant c, as shown in Figure 8. Because of the small coordination number and less hybridization with O 2p of Co out-of-plane, the bandwidth is mainly controlled by the Co−O−Co bond angle and the Co−O bond length in the octahedron in plane. It can be seen from Figure 8 that the in-plane bond angles weakly depend on the strain, whereas the bond lengths decrease as the compressive strain increases in the octahedral.

To get more quantitative information, we performed the DFT calculation to map out the electronic structure of two different lattice constants of the BM-SCO2.5 thin films and the SrCoO2.75 thin film. Figure 9 shows the total and projected DOS onto O 2p, Co-tetrahedral 3d and Co-octahedral 3d for two different c lattice-constant BM-SCO2.5 thin films and SrCoO2.75 thin films. From Figure 9 a,b, we can see that for the SrCoO2.5 thin film, without the variation of oxygen content, with the larger lattice constant c, the decrease of the Co−O bond length in the octahedral does not make a big difference to the energy band gap. With the decrease of the film thickness, the in-compressive strain is accompanied by an increase of oxygen content, which we can see from the STEM results. Therefore, the decrease of the energy band gap with the decrease of the film thickness is due to the increase of oxygen content rather than the in-plane compressive strain. Therefore, the proposal that the electronic structure of the BM-SCO2.5 thin films can be tuned by the interfacial strain accompanied by an increase of the oxygen content was confirmed by the experiments and the theoretical calculations.

4. CONCLUSIONS

In summary, a series of BM-SCO2.5 thin films with the different thicknesses on the LAO substrate were grown by PLD. With the increase of the film thickness, the in-plane compressive strain due to the lattice mismatch releases, the c-axis lattice constant decreases. In this process, the Raman spectra undergo a substantial softening and make a big difference to the energy band gap of BM-SCO2.5. Because of the relaxation of compressive strain, the Co−O bond length increases, which does not make a big difference to the energy band gap. With the decrease of the film thickness, the interfacial strain is accompanied by an increase of oxygen content, resulting in the decrease of energy band gap. This observation provides a new way to design new functional oxides for many technological applications, such as for cathodes in solid oxide fuel cells using strain as a key adjustable parameter.

■ ASSOCIATED CONTENT

Supporting Information

The Supporting Information is available free of charge on the ACS Publications website at DOI: 10.1021/acsami.8b00791.

Magnetization as a function of temperature for the 187 nm-thick SCO2.5 thin film measured at field-cooled mode in a magnetic field of 1000 Oe; resistivity versus temperature for the 187 nm-thick SCO2.5 film; XRD $\theta-2\theta$ patterns of c-axis-oriented BM-SCO2.5 films epitaxially grown on the (001) LAO substrate; XRD $\theta-2\theta$ patterns of the BM-SCO2.5 films on (001) LAO substrates with different thicknesses; variation of fwhm of (008) peak with the film thicknesses; STEM image of the 187 nm-thick SCO2.5 film; Raman spectra of the 32 nm-thick SCO2.5 thin film measured at different temperatures and temperature-dependent Raman peak positions of 450, 650, and 690 cm^{-1} modes; optical absorption spectra obtained from transmittance measurements of the SrCoO2.5 thin films with different thicknesses; comparison of the functionals (LDA, PBE, and PBEsol) and various U values; and relationship of the lattice constants and band gaps (PDF)

■ AUTHOR INFORMATION

Corresponding Authors

*E-mail: hguo@zzu.edu.cn (H.G.).
*E-mail: kjjin@iphy.ac.cn (K.-j.J.).
*E-mail: kurash@ihep.ac.cn (K.I.).

ORCID

Haizhong Guo: 0000-0002-6128-4225
Lin Gu: 0000-0002-7504-031X
Xiaolong Li: 0000-0002-1674-9345
Kui-juan Jin: 0000-0002-0047-4375
Tieying Yang: 0000-0002-4728-7438
Youwen Long: 0000-0002-8587-7818

Author Contributions

The manuscript was written through contributions of all authors. All authors have given approval to the final version of the manuscript. H.Z.G. designed this work. J.L.Z. and H.Z.G. grew the samples. J.L.Z., T.Y.Y., X.L.L., and Y.L. performed the XRD and grazing incidence XRD measurements. Q.H.Z. and L.G. performed the STEM measurements. J.L.Z. performed Raman and optical absorption spectra measurements. X.H. performed the calculations. J.L.Z. and H.Z.G. wrote the manuscript. All contributed discussions.

Funding

National Key Basic Research Program of China (grant nos. 2013CB328706 and 2014CB921001), the National Key Research and Development Program of China grant No.

DOI: 10.1021/acsami.8b00791
ACS Appl. Mater. Interfaces 2018, 10, 10211−10219

2016YFA0401002, the National Natural Science Foundation of China (grant nos. 11574365, 11474349, 11674385, 11404380, 11574408, and 11375228), the Key Research Program of Frontier Sciences of the Chinese Academy of Sciences (grant no. QYZDJ-SSW-SLH020), and the Strategic Priority Research Program (B) of the Chinese Academy of Sciences (grant No. XDB07030200).

Notes

The authors declare no competing financial interest.

■ ACKNOWLEDGMENTS

This work was supported by the National Key Basic Research Program of China (grant nos. 2013CB328706 and 2014CB921001), the National Key Research and Development Program of China grant no. 2016YFA0401002, the National Natural Science Foundation of China (grant nos. 11574365, 11474349, 11674385, 11404380, 11574408, and 11375228), the Key Research Program of Frontier Sciences of the Chinese Academy of Sciences (grant no. QYZDJ-SSW-SLH020), and the Strategic Priority Research Program (B) of the Chinese Academy of Sciences (grant no. XDB07030200). The authors would like to thank BL14B1 beam line of Shanghai Synchrotron Radiation Facility for technique support.

■ ABBREVIATIONS

TMOs, transition-metal oxides; BM, brownmillerite; SCO2.5, $SrCoO_{2.5}$; PLD, pulsed laser deposition; STO, $SrTiO_3$; LAO, $LaAlO_3$; LSAT, $(LaAlO_3)_{0.3}-(SrAlTaO_3)_{0.7}$; XRD, X-ray diffractometry; STEM, scanning tunneling electron microscopy

■ REFERENCES

(1) Tokura, Y.; Nagaosa, N. Orbital Physics in Transition-Metal Oxides. *Science* **2000**, *288*, 462−468.

(2) Kalinin, S. V.; Spaldin, N. A. Functional Ion Defects in Transition Metal Oxides. *Science* **2013**, *341*, 858−859.

(3) Guo, H.; Li, Q.; Yang, Z.; Jin, K.-j.; Ge, C.; Gu, L.; He, X.; Li, X.; Zhao, R.; Wan, Q.; Wang, J.; He, M.; Wang, C.; Lu, H.; Yang, Y.; Yang, G. Manipulating Magnetoelectric Properties by Interfacial Coupling in $La_{0.3}Sr_{0.7}MnO_3/Ba_{0.7}Sr_{0.3}TiO_3$ superlattices. *Sci. Rep.* **2017**, *7*, 7693.

(4) Biškup, N.; Salafranca, J.; Mehta, V.; Oxley, M. P.; Suzuki, Y.; Pennycook, S. J.; Pantelides, S. T.; Varela, M. Insulating Ferromagnetic $LaCoO_{3-\delta}$ Films: A Phase Induced by Ordering of Oxygen Vacancies. *Phys. Rev. Lett.* **2014**, *112*, 087202.

(5) Mefford, J. T.; Hardin, W. G.; Dai, S.; Johnston, K. P.; Stevenson, K. J. Anion Charge Storage Through Oxygen Intercalation in $LaMnO_3$ Perovskite Pseudocapacitor Electrodes. *Nat. Mater.* **2014**, *13*, 726−732.

(6) Tambunan, O. T.; Parwanta, K. J.; Acharya, S. K.; Lee, B. W.; Jung, C. U.; Kim, Y. S.; Park, B. H.; Jeong, H.; Park, J.-Y.; Cho, M. R.; Park, Y. D.; Choi, W. S.; Kim, D.-W.; Jin, H.; Lee, S.; Song, S. J.; Kang, S.-J.; Kim, M.; Hwang, C. S. Resistance Switching in Epitaxial $SrCoO_x$ Thin Films. *Appl. Phys. Lett.* **2014**, *105*, 063507.

(7) Zhang, K. H. L.; Sushko, P. V.; Colby, R.; Du, Y.; Bowden, M. E.; Chambers, S. A. Reversible Nano-Structuring of $SrCrO_{3-\delta}$ through Oxidation and Reduction at Low Temperature. *Nat. Commun.* **2014**, *5*, 4669.

(8) Jeen, H.; Bi, Z.; Choi, W. S.; Chisholm, M. F.; Bridges, C. A.; Paranthaman, M. P.; Lee, H. N. Orienting Oxygen Vacancies for Fast Catalytic Reaction. *Adv. Mater.* **2013**, *25*, 6459−6463.

(9) Huang, S.; Feng, S.; Lu, Q.; Li, Y.; Wang, H.; Wang, C. Cerium and Niobium Doped SrCoO3−δ as a Potential Cathode for Intermediate Temperature Solid Oxide Fuel Cells. *J. Power Sources* **2014**, *251*, 357−362.

(10) Kim, Y.-M.; He, J.; Biegalski, M. D.; Ambaye, H.; Lauter, V.; Christen, H. M.; Pantelides, S. T.; Pennycook, S. J.; Kalinin, S. V.; Borisevich, A. Y. Probing Oxygen Vacancy Concentration and Homogeneity in Solid-Oxide Fuel-Cell Cathode Materials on the Subunit-Cell Level. *Nat. Mater.* **2012**, *11*, 888−894.

(11) Sengodan, S.; Choi, S.; Jun, A.; Shin, T. H.; Ju, Y.-W.; Jeong, H. Y.; Shin, J.; Irvine, J. T. S.; Kim, G. Layered Oxygen-Deficient Double Perovskite as an Efficient and Stable Anode for Direct Hydrocarbon Solid Oxide Fuel Cells. *Nat. Mater.* **2015**, *14*, 205−209.

(12) Auckett, J. E.; Studer, A. J.; Pellegrini, E.; Ollivier, J.; Johnson, M. R.; Schober, H.; Miiller, W.; Ling, C. D. Combined Experimental and Computational Study of Oxide Ion Conduction Dynamics in $Sr_2Fe_2O_5$ Brownmillerite. *Chem. Mater.* **2013**, *25*, 3080−3087.

(13) Cascos, V.; Martínez-Coronado, R.; Alonso, J. A.; Fernández-Díaz, M. T. Visualization by Neutron Diffraction of 2D Oxygen Diffusion in the Sr(0.7)Ho(0.3)CoO(3-delta) Cathode for Solid-Oxide Fuel Cells. *ACS Appl. Mater. Interfaces* **2014**, *6*, 9194−9200.

(14) Muchuweni, E.; Sathiaraj, T. S.; Nyakotyo, H. Synthesis and Characterization of Zinc Oxide Thin films for Optoelectronic Applications. *Heliyon* **2017**, *3*, No. e00285.

(15) Climent-Pascual, E.; Hames, B. C.; Moreno-Ramírez, J. S.; Álvarez, A. L.; Juarez-Perez, E. J.; Mas-Marza, E.; Mora-Seró, I.; de Andrés, A.; Coya, C. Influence of the Substrate on the Bulk Properties of Hybrid Lead Halide Oerovskite Films. *J. Mater. Chem. A* **2016**, *4*, 18153−18163.

(16) Opasanont, B.; Van, K. T.; Kuba, A. G.; Choudhury, K. R.; Baxter, J. B. Adherent and Conformal Zn(S, O,OH) Thin Films by Rapid Chemical Bath Deposition with Hexamethylenetetramine Additive. *ACS Appl. Mater. Interfaces* **2015**, *7*, 11516−11525.

(17) Guerrero, A.; Garcia-Belmonte, G.; Mora-Sero, I.; Bisquert, J.; Kang, Y. S.; Jacobsson, T. J.; Correa-Baena, J.-P.; Hagfeldt, A. Properties of Contact and Bulk Impedances in Hybrid Lead Halide Perovskite Solar Cells Including Inductive Loop Elements. *J. Phys. Chem. C* **2016**, *120*, 8023−8032.

(18) Erba, A.; Ruggiero, M. T.; Korter, T. M.; Dovesi, R. Piezo-optic Tensor of Crystals from Quantum-Mechanical Calculations. *J. Chem. Phys.* **2015**, *143*, 144504.

(19) Berger, D.; de Moura, A. P.; Oliveira, L. H.; Bastos, W. B.; La Porta, F. A.; Rosa, I. L. V.; Li, M. S.; Tebcherani, S. M.; Longo, E.; Varela, J. A. Improved Photoluminescence Emission and Gas Sensor Properties of ZnO Thin Films. *Ceram. Int.* **2016**, *42*, 13555−13561.

(20) Oliveira, L. H.; Ramírez, M. A.; Ponce, M. A.; Ramajo, L. A.; Albuquerque, A. R.; Sambrano, J. R.; Longo, E.; Castro, M. S.; La Porta, F. A. Optical and Gas-sensing Properties, and Electronic Structure of the Mixed-Phase $CaCu_3Ti_4O_{12}/CaTiO_3$ Composites. *Mater. Res. Bull.* **2017**, *93*, 47−55.

(21) Zhang, Z.; Andre, L.; Abanades, S. Experimental Assessment of Oxygen Exchange Capacity and Thermochemical Redox Cycle Behavior of Ba and Sr Series Perovskites for Solar Energy Storage. *Sol. Energy* **2016**, *134*, 494−502.

(22) Mueller, D. N.; Machala, M. L.; Bluhm, H.; Chueh, W. C. Redox Activity of Surface Oxygen Anions in Oxygen-Deficient Perovskite Oxides During Electrochemical Reactions. *Nat. Commun.* **2015**, *6*, 6097.

(23) Song, G.; Zhang, W. First-principles Study on the Phase Diagram and Multiferroic Properties of $(SrCoO_3)_1/(SrTiO_3)_1$ Superlattices. *Sci. Rep.* **2014**, *4*, 4564.

(24) Qiao, L.; Xiao, H. Y.; Meyer, H. M.; Sun, J. N.; Rouleau, C. M.; Puretzky, A. A.; Geohegan, D. B.; Ivanov, I. N.; Yoon, M.; Weber, W. J.; Biegalski, M. D. Nature of the Band Gap and Origin of the Electro-/Photo-Activity of Co3O4. *J. Mater. Chem. C* **2013**, *1*, 4628−4633.

(25) Mulinari, T. A.; La Porta, F. A.; Andrés, J.; Cilense, M.; Varela, J. A.; Longo, E. Microwave-Hydrothermal Synthesis of Single-Crystalline Co_3O_4 Spinel Nanocubes. *CrystEngComm* **2013**, *15*, 7443−7449.

(26) Hu, S.; Seidel, J. Oxygen Content Mmodulation by Nanoscale Chemical and Electrical Patterning in Epitaxial $SrCoO_{3-\delta}$ ($0 < \delta \leq 0.5$) Thin Films. *Nanotechnology* **2016**, *27*, 325301.

(27) Lu, Q.; Yildiz, B. Voltage-Controlled Topotactic Phase Transition in Thin-Film $SrCoO_x$ Monitored by In Situ X-ray Diffraction. *Nano Lett.* **2016**, *16*, 1186−1193.

DOI: 10.1021/acsami.8b00791
ACS Appl. Mater. Interfaces 2018, 10, 10211−10219

(28) Lu, Q.; Chen, Y.; Bluhm, H.; Yildiz, B. Electronic Structure Evolution of SrCoOx during Electrochemically Driven Phase Transition Probed by in Situ X-ray Spectroscopy. *J. Phys. Chem. C* **2016**, *120*, 24148−24157.
(29) Jeen, H.; Choi, W. S.; Biegalski, M. D.; Folkman, C. M.; Tung, I.-C.; Fong, D. D.; Freeland, J. W.; Shin, D.; Ohta, H.; Chisholm, M. F.; Lee, H. N. Reversible Redox Reactions in an Epitaxially Stabilized SrCoO(x) Oxygen Sponge. *Nat. Mater.* **2013**, *12*, 1057−1063.
(30) Ichikawa, N.; Iwanowska, M.; Kawai, M.; Calers, C.; Paulus, W.; Shimakawa, Y. Reduction and Oxidation of $SrCoO_{2.5}$Thin Films at Low Temperatures. *Dalton Trans.* **2012**, *41*, 10507−10510.
(31) Jeen, H.; Choi, W. S.; Freeland, J. W.; Ohta, H.; Jung, C. U.; Lee, H. N. Topotactic Phase Transformation of the Brownmillerite $SrCoO_{2.5}$ to the Perovskite $SrCoO_{3-\delta}$. *Adv. Mater.* **2013**, *25*, 3651−3656.
(32) Choi, W. S.; Jeen, H.; Lee, J. H.; Seo, S. S.; Cooper, V. R.; Rabe, K. M.; Lee, H. N. Reversal of the Lattice Structure in SrCoO(x) Epitaxial Thin Films Studied by Real-Time Optical Spectroscopy and First-Principles Calculations. *Phys. Rev. Lett.* **2013**, *111*, 097401.
(33) Lu, N.; Zhang, P.; Zhang, Q.; Qiao, R.; He, Q.; Li, H. B.; Wang, Y.; Guo, J.; Zhang, D.; Duan, Z.; Li, Z.; Wang, M.; Yang, S.; Yan, M.; Arenholz, E.; Zhou, S.; Yang, W.; Gu, L.; Nan, C.-W.; Wu, J.; Tokura, Y.; Yu, P. Electric-field Control of Tri-State Phase Transformation with a Selective Dual-Ion Switch. *Nature* **2017**, *546*, 124−128.
(34) Zhang, Q.; He, X.; Shi, J.; Lu, N.; Li, H.; Yu, Q.; Zhang, Z.; Chen, L.-Q.; Morris, B.; Xu, Q.; Yu, P.; Gu, L.; Jin, K.; Nan, C.-W. Atomic-Resolution Imaging of Electrically Induced Oxygen Vacancy Migration and Phase Transformation in $SrCoO_{2.5-\delta}$. *Nat. Commun.* **2017**, *8*, 104.
(35) Vashook, V.; Zinkevich, M. V.; Zonov, Y. G. Phase Relations in Oxygen-Deficient $SrCoO_{2.5-\delta}$. *Solid State Ionics* **1999**, *116*, 129−138.
(36) Mitra, C.; Meyer, T.; Lee, H. N.; Reboredo, F. A. Oxygen Diffusion Pathways in Brownmillerite $SrCoO_{2.5}$: Influence of Structure and Chemical Potential. *J. Chem. Phys.* **2014**, *141*, 084710.
(37) Paulus, W.; Schober, H.; Eibl, S.; Johnson, M.; Berthier, T.; Hernandez, O.; Ceretti, M.; Plazanet, M.; Conder, K.; Lamberti, C. Lattice Dynamics to Trigger Low Temperature Oxygen Mobility in Solid Oxide Ion Conductors. *J. Am. Chem. Soc.* **2008**, *130*, 16080−16085.
(38) Mefford, J. T.; Rong, X.; Abakumov, A. M.; Hardin, W. G.; Dai, S.; Kolpak, A. M.; Johnston, K. P.; Stevenson, K. J. Water Electrolysis on $La_{1-x}Sr_xCoO_{3-delta}$ Perovskite Electrocatalysts. *Nat. Commun.* **2016**, *7*, 11053.
(39) Guo, H.; Zhao, R.; Jin, K.-j.; Gu, L.; Xiao, D.; Yang, Z.; Li, X.; Wang, L.; He, X.; Gu, J.; Wan, Q.; Wang, C.; Lu, H.; Ge, C.; He, M.; Yang, G. Interfacial-Strain-Induced Structural and Polarization Evolutions in Epitaxial Multiferroic $BiFeO_3$ (001) Thin Films. *ACS Appl. Mater. Interfaces* **2015**, *7*, 2944−2951.
(40) Christen, H. M.; Nam, J. H.; Kim, H. S.; Hatt, A. J.; Spaldin, N. A. Stress-Induced R-MA-MC-T Symmetry Changes in $BiFeO_3$ Films. *Phys. Rev. B: Condens. Matter Mater. Phys.* **2011**, *83*, 144107.
(41) Petrie, J. R.; Jeen, H.; Barron, S. C.; Meyer, T. L.; Lee, H. N. Enhancing Perovskite Electrocatalysis through Strain Tuning of the Oxygen Deficiency. *J. Am. Chem. Soc.* **2016**, *138*, 7252−7255.
(42) Petrie, J. R.; Mitra, C.; Jeen, H.; Choi, W. S.; Meyer, T. L.; Reboredo, F. A.; Freeland, J. W.; Eres, G.; Lee, H. N. Strain Control of Oxygen Vacancies in Epitaxial Strontium Cobaltite Films. *Adv. Funct. Mater.* **2016**, *26*, 1564−1570.
(43) Choi, W. S.; Kwon, J.-H.; Jeen, H.; Hamann-Borrero, J. E.; Radi, A.; Macke, S.; Sutarto, R.; He, F.; Sawatzky, G. A.; Hinkov, V.; Kim, M.; Lee, H. N. Strain-induced Spin States in Atomically Ordered Cobaltites. *Nano Lett.* **2012**, *12*, 4966−4970.
(44) Meyer, T. L.; Jeen, H.; Gao, X.; Petrie, J. R.; Chisholm, M. F.; Lee, H. N. Symmetry-Driven Atomic Rearrangement at a Brownmillerite-Perovskite Interface. *Adv. Electron. Mater.* **2016**, *2*, 1500201.
(45) Lee, J. H.; Rabe, K. M. Coupled Magnetic-Ferroelectric Metal-Insulator Transition in Epitaxially Strained $SrCoO_3$ from First Principles. *Phys. Rev. Lett.* **2011**, *107*, 067601.
(46) La Porta, F. A.; Andrés, J.; Li, M. S.; Sambrano, J. R.; Varela, J. A.; Longo, E. Zinc Blende Versus Wurtzite ZnS Nanoparticles: Control of the Phase and Optical Properties by Tetrabutylammonium Hydroxide. *Phys. Chem. Chem. Phys.* **2014**, *16*, 20127−20137.
(47) Muñoz, A.; de la Calle, C.; Alonso, J. A.; Botta, P. M.; Pardo, V.; Baldomir, D.; Rivas, J. Crystallographic and Magnetic Structure of $SrCoO_{2.5}$ Brownmillerite: Neutron Study Coupled with Band-Structure Calculations. *Phys. Rev. B: Condens. Matter Mater. Phys.* **2008**, *78*, 054404.
(48) Sullivan, E.; Hadermann, J.; Greaves, C. Crystallographic and magnetic characterisation of the brownmillerite Sr2Co2O5. *J. Solid State Chem.* **2011**, *184*, 649−654.
(49) Glamazda, A.; Choi, K.-Y.; Lemmens, P.; Choi, W. S.; Jeen, H.; Meyer, T. L.; Lee, H. N. Structural Instability of the CoO_4Tetrahedral Chain in $SrCoO_{3-\delta}$Thin Films. *J. Appl. Phys.* **2015**, *118*, 085313.
(50) Sherwood, P. M. A. Vibrational spectroscopy of solids. *CUP Archive*: **1972**, DOI: 10.1002/ange.19740860415.
(51) Granado, E.; García, A.; Sanjurjo, J. A.; Rettori, C.; Torriani, I. Magnetic Ordering Effects in the Raman Spectra of $La_{1-x}Mn_{1-x}O_3$. *Phys. Rev. B: Condens. Matter Mater. Phys.* **1999**, *60*, 11879.

DOI: 10.1021/acsami.8b00791
ACS Appl. Mater. Interfaces 2018, 10, 10211−10219